POLITECNICO DI TORINO
Repository ISTITUZIONALE

Wall bounded flows manipulation using sinusoidal riblets

(Article begins on next page)

08 November 2022

Wall bounded flows manipulation using sinusoidal riblets

Gioacchino Cafiero*, Enrico Amico† and Gaetano Iuso‡
Politecnico di Torino, Corso Duca degli Abruzzi 24, Torino, 10129

We experimentally investigate the effects of microgrooves on the development of a zero pressure gradient turbulent boundary layer. Starting from the well-known streamwise aligned riblets, we look at the effect of wavy riblets, characterized by a sinusoidal pattern in the mean flow direction. We perform hot wire experiments as well as particle image velocimetry to get some insights on the effect of the sinusoidal shape on the near wall organisation of the boundary layer. The statistical analysis clearly shows that the wavy pattern has a strong influence on the near wall structure of the boundary layer. The statistical analysis performed using the VITA technique reveals that the coherent structures that characterize the turbulent boundary layer are attenuated by the geometry manipulation. Furthermore, the POD reconstructed velocity fields, measured with PIV, reveal that the manipulation tampers with the momentum exchange occurring between the near wall and the outer region of the boundary layer, hence suggesting a modified turbulence production cycle.

I. Nomenclature

a	=	amplitude of the sinusoidal riblet
h	=	height of the groove
H	=	shape factor of the boundary layer
l_τ	=	viscous unit
Re_θ	=	$U_\infty \theta / \nu$ Reynolds number based on the momentum thickness
Re_τ	=	$u_\tau \delta / \nu$ friction Reynolds number
s	=	spacing between grooves
u	=	streamwise velocity
v	=	wall normal velocity
$\overline{u'^2}$	=	rms of the streamwise velocity
$\overline{u'^2}_{ev}$	=	rms of the streamwise velocity relative to the VITA events
$\hat{u}'$	=	Conditionally averaged streamwise velocity
u_τ	=	friction velocity
U_∞	=	freestream speed
x	=	streamwise coordinate
y	=	wall normal coordinate
λ	=	wavelength of the sinusoidal riblet
δ	=	boundary layer thickness
θ	=	momentum thickness

II. Introduction

$\mathbf{T}$HE study of zero pressure gradient turbulent boundary layers has represented one of the driving forces for research in fluid dynamics. One of the key drivers has been the definition of efficient flow control techniques to reduce the skin friction drag. Passive methodologies, i.e. not requiring any power supplied to the system, have shown interesting results both in boundary layers [1] as well as to reduce the induced drag [2] or increase the convective heat transfer rate [3] of impinging jets, to cite some examples.

*Assistant Professor, Department of Mechanical and Aerospace Engineering, Politecnico di Torino, Corso Duca degli Abruzzi 24, AIAA Member.
†Research Student, Department of Mechanical and Aerospace Engineering, Politecnico di Torino, Corso Duca degli Abruzzi 24
‡Full Professor, Department of Mechanical and Aerospace Engineering, Politecnico di Torino, Corso Duca degli Abruzzi 24, AIAA Member.

Active solutions, on the other hand, require a dedicated power supply, but can achieve significantly larger values of drag reduction. Examples are not limited to the skin friction drag reduction [4, 5], but also to the control of separated flows [6].

Among the passive solutions, one of the most promising that has been proposed in the past is providing permanent geometry manipulations to the wall, through micro-grooves. These grooves are generally referred to as riblets [7–9].

The key parameters of the riblet geometry are represented by the depth of the micro-groove, the spacing between the grooves and its cross-section. An extensive parametric study carried out by [10] has shown that blade riblets aligned to the streamwise direction yield the highest drag reduction, but parabolic shaped profiles could respond better to the ease of manufacturing for realistic application.

A non-dimensional riblet spacing ($s^+ = su_\tau/\nu$, with u_τ being the friction velocity and ν the kinematic viscosity; with the superscript + we indicate the scaling in inner units) of approximately 15-16 demonstrated the highest values of drag reduction. More recently, [11] introduced a dimensionless parameter, $l_g^+ = (A_g^+)^{1/2}$, accounting for the cross section area (A_g^+) of the riblet profile as well. The authors showed that the highest drag reduction would be obtained for values of $l_g^+ \approx 11$.

The underlying mechanisms leading to drag reduction has been addressed in the literature by [12] and [13], among others, through highly resolved direct numerical simulation of triangular riblets. The authors showed that the optimal value of the spacing corresponds to the condition where the near wall structures cannot fit within the groove; hence, the structures are displaced towards the outer layers of the boundary layer. Near the wall, a region of nearly stagnating flow is then produced, with corresponding reduction of the wall shear stress and skin friction drag.

Further improvements to the optimal riblet geometry have been proposed over the years. Bio-inspired geometries [14], zigzag geometries [15] and wavy patterns [16–19]. The latter solution is based on the possibility of enjoying the benefits brought by the riblet geometry with those related to active flow control mechanisms, such as the spanwise oscillation of the wall [20], or forced by the tangential injection of momentum [4, 21].

Despite showing interesting results, a statistical description of the near wall structure stemming from the wavy modification of the wall (henceforth referred to as sinusoidal riblets) has not been performed yet.

In this manuscript we show the effect of the riblet geometry manipulation through the statistical analysis of the experimental data collected using hot wire anemometry and particle image velocimetry. In section III we provide a description of the experimental apparatus and of the measurement techniques; in section IV we report the main findings obtained through the statistical analysis of the hot wire and PIV data. Finally we draw our conclusions in section V.

III. Experimental apparatus

The experiments were performed in an open circuit wind tunnel at Politecnico di Torino. The tunnel has a settling chamber containing honeycomb and mesh screens, followed by a contraction with area ratio of 3:1, leading into a test section 5300 mm long and with a cross-section area of 500 mm x 700 mm.

The flat plate where the boundary layer develops is located at mid-height of the test section and extends from its side to side, thus effectively reducing the cross section area to 500 mm x 350 mm. This reduction is obtained through a contoured contraction. The purpose of this is twofold: first it avoids any sharp area variation, which would disrupt the quality of the flow. Second, it allows for the insulation of the bottom portion of the test section which is used for the plate positioning system. A trip wire is placed at the start of the flat plate to trigger an early transition to a turbulent boundary layer.

A portion of the flat plate of size 260 mm x 260 mm is hollow and allows for the positioning of different plates. The correct alignment of the tested plate with respect to the remaining portion of the flat plate is ensured with micrometric accuracy through the possibility of controlling the height and the inclination of the tested plate. In particular, the height is controlled using a laser optical displacement measurement optoNCDT 1320 manufactured by Micro-Epsilon, whilst the inclination is checked through a high precision digital inclinometer.

The alignment of the mounted plate to the surrounding flat plate is performed through the combination of the high precision laser and a calibrated flat plate. The vertical positioning of the riblet plate is changed with micrometric accuracy using a stepper motor. The plate is considered aligned when it touches the calibrated glass plate. The reading of the laser displacement measurement is considered as the datum.

Four different plates were investigated: a flat plate, a riblet plate with longitudinal grooves (RLONG), two riblet plates with sinusoidal grooves (RS1 and RS2). Each one of the tested plates is a square having side of 258 mm and thickness of 10 mm. This leads to a small gap between the edge of the tested plate and the flat plate. A labyrinth seal was mounted underneath the plate to avoid any leakage through the gap between the tested plate and the flat plate.
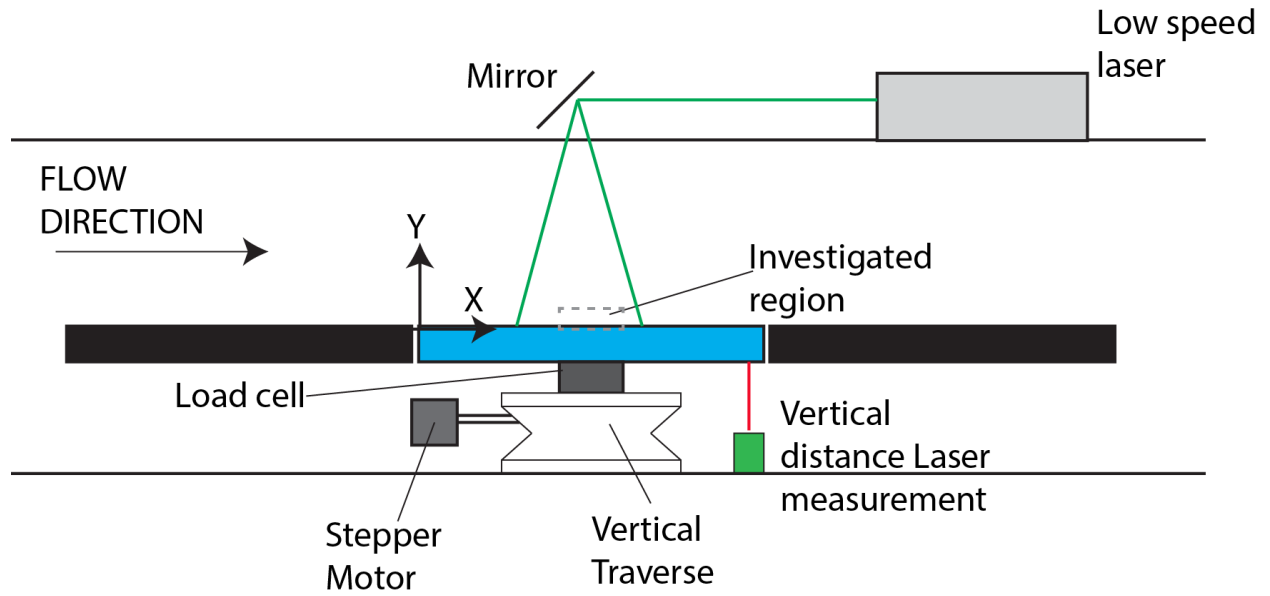
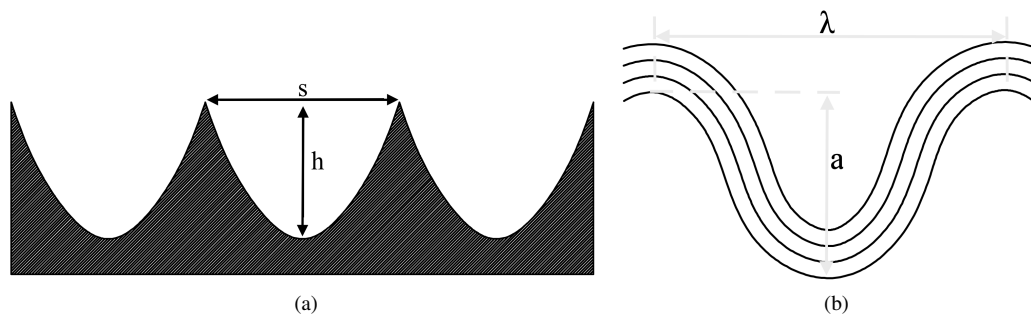**Fig. 1   Schematic representation of the test section with detail of the removable plate.**

Fig. 2   Detail of the parabolic profile of the grooves.

3

	RLONG	RS1	RS2
s (mm)	0.30	0.30	0.30
h (mm)	0.21	0.21	0.21
h/s	0.70	0.70	0.70
a (mm)	0	0.15	0.60
λ (mm)	∞	19.2	19.2
N_λ	N.A.	13	13

Table 1   Geometric data for the riblet plates.

$U_\infty(m/s)$	$u_\tau(m/s)$	Re_τ	Re_θ	$\delta(mm)$	$l_\tau(\mu m)$	H
13.4	0.53	1210	2800	34.5	28.4	1.34

Table 2   Experiment details: value of the asymptotic speed U_∞, friction velocity u_τ, Reynolds numbers based on friction velocity Re_τ and momentum thickness Re_θ, boundary layer thickness δ, viscous lengthscale l_τ and boundary layer shape factor H.

The three riblet plates are characterized by the same groove profile, having parabolic shape. The height of the groove is $h=210\mu m$ whilst the spacing between two grooves is $s=300\mu m$, thus resulting in a h/s ratio equal to 0.7 (see Figure 2a). The two sinusoidal riblets are characterized by the same wavelength $\lambda=19.2$mm, thus leading to at least $N_\lambda=13$ wavelengths on the tested plate; conversely, two different values of the amplitude a are considered (see Figure 2b), with $a=0.15$mm in the RS1 and $a=0.6$mm in the RS2 case, respectively. A summary of the geometric parameters of the riblet plates is reported in table 1.

The riblet performance is strongly depending on the spacing normalised in inner units $s^+ = s/l_\tau$, where $l_\tau = \nu/u_\tau$ is the viscous lengthscale, ν the air kinematic viscosity and u_τ is the friction velocity. Since the manufacturing of the riblet plates can be expensive, we vary s^+ by changing the Reynolds number, although the results of only one value of the Reynolds number are reported here.

The freestream speed U_∞ is measured using a Pitot tube located at the inlet of the test section and connected to a pressure transducer Setra 239C having a FS 0.2psi and ±0.14% accuracy. The resulting typical error on the measurement of the freestream speed is ±1%. The value of the investigated friction Reynolds number ($Re_\tau = u_\tau\delta/\nu$, with δ being the boundary layer thickness) is 1210. Details of the experiment conditions are listed in table 2. The value of the friction velocity u_τ is obtained from a Clauser fit to the logarithmic portion of the mean flow profile (using as values of the constants $k = 0.41$ and $B = 5.2$).

A. Measurement techniques

The flow field was characterized using both hot wire anemometry (HWA) and low speed Particle Image Velocimetry (PIV).

In the HWA experiments, the velocity signal is measured using a one component hot wire driven by a Dantec DISA constant temperature anemometer (CTA). The hot wire was operated with an overheat ratio of 0.8. The sensing length of the wire is $l \approx 1\ mm$, corresponding to $l^+ \approx 40$ whilst the wire diameter is $5\mu m$. As indicated by [22], this value of l^+ may lead to the modulation of the streamwise turbulence intensity.

Data are sampled at a frequency of 20 KHz using a 16-bit National Instruments NI-9215 data acquisition card. Each measurement lasts for $t_a=60s$. This was estimated to be a sufficiently long time for convergence of the turbulent statistics studied here.

The spatial organization of the flow was investigated through low speed planar PIV. A Dantec Dynamics Nd:YAG Dual Power 200 laser (200 mJ/pulse energy, 15 Hz repetition rate) operated in dual pulse mode was used to illuminate the tracing particles. The laser was mounted on the roof of the wind tunnel and illuminated a region extending for about 25mm in the streamwise direction (xy plane), centred with respect to the removable plate.

One Andor Zyla 5.5Mpix sCMOS camera (sensor size of 2560x2160 pix, pixel size of 6.5 μm) was used to capture

the images of the tracing particles. The camera was synchronized with the laser system and operated in double exposure mode. The acquisition frequency was set to 15 Hz. The camera was equipped with a Nikon 200mm Micro lens, operated at a value of the aperture $f_\# = 11$. The imaged area extended for 23x21 mm in both cases ($x - y$ and $x - z$ planes), corresponding to a spatial resolution of approximately 80 pix/mm.

The flow was seeded upstream of the stagnation chamber using Fog Fluid 'Extra Clean'. The liquid small droplets of $1\ \mu m$ in diameter were generated using a Safex Fog generator FOG 2010. For each Reynolds number and each plate 2000 double exposure images were acquired. The raw images were pre-processed to reduce to a minimum the reflection of the laser onto the flat plate. The Proper Orthogonal Decomposition based approach, as proposed by [23], allowed for a significant attenuation of the laser reflection on the removable plate.

The vector fields were obtained by processing the collected images using a correlation based algorithm. A spline interpolation of the image and of the velocity field was performed, as recommended by [24, 25]. A Blackmann weighting window was used to tune the spatial resolution [26]. The algorithm is based on a multi-pass approach and the final interrogation window size was 16x16 pix, with 87.5% overlap, in the case of the streamwise experiments and 48x48 pix, with 75% overlap in the case of the wall parallel experiments.

IV. Results

We focus on the statistical analysis of the flow field by looking primarily at the variable interval time averaging technique, which allows us to determine the existence of near wall events [27]. We can define a local variance, $var_{loc}(x, y, t, T)$, as

$$var_{loc}(x, y, t, T) = \hat{u'^2}(x, y, t, T) - (\hat{u'}(x, y, t, T))^2 \tag{1}$$

where the $\hat{}$ indicates a local average, i.e. an average performed over the time interval T, which is typically set to $T^+ = 10$.

The detection criterion dictates that an event is obtained when the value of the local variance $var_{loc}(x, y, t, T)$, exceeds by a factor k the value of the global variance ($\overline{u'^2} = \lim_{T \to \infty} var_{loc}$), that we set to $k = 1$. Among all those events that meet this criterion, we select those that are characterized by $du'/dt > 0$, that we can identify as acceleration events.

The time t_j where the previous conditions are met allows us to determine the conditionally averaged velocity signal as:

$$\hat{u}(x, y, \tau) = \frac{1}{N} \sum_{j=1}^{N} u'(y, t_j + \tau) \tag{2}$$

Figure 3a shows the accelerated event represented as conditionally averaged streamwise velocity. The data show that the sinusoidal riblets clearly act in a way to attenuate the velocity jump across the event. As evidenced by [4], the VITA events are located at the edges of the low-speed and high-speed velocity streaks. It can then be argued that the riblet geometry reduces the streamwise velocity gradients. This is further confirmed by the pdf of the velocity jump calculated across VITA events at $y^+ = 10$. The data show that all the riblet cases are typically characterized by lower values of Δu; furthermore, the peak of the pdf, is typically shifted towards low values of the Δu.

Figure 4a shows the pdf of the velocity fluctuations calculated on the entire signal (a) and only on those portions of the signal where a VITA event is detected (b). The velocity variance associated with the VITA events are typically much more intense than the global variance. All the riblet cases are characterized by an attenuation of the velocity variance, with respect to the smooth case. In particular, the RLONG and RS1 cases are those responsible for the most clear reduction, with a shift of the pdf peak of about 10%.

Further details about the effect of the geometry manipulation on the near wall structure of the boundary layer can be obtained from the Wavelet transform of the velocity signals measured with the hot wire. The wavelet transform is a powerful tool that allows the description of the flow behavior in the time-frequency domain. A complete overview of the wavelet transform is beyond the scope of this paper and can be found in [28].

Figure 5a-d shows the colormaps of the Wavelet coefficients for the four investigated cases in the time-frequency domain. The contour refers to only a small portion of the overall velocity signal, namely 0.3s corresponding to a $\Delta t^+ = \approx 5600$. A qualitative comparison immediately allows to draw a first conclusion: the riblet cases attenuate the energy intensity across the entire range of the investigated frequencies. It is interesting to notice that the Smooth case (figure 5a) features coherent energy containing structures at multiple scales, which are instead mitigated in the case of the riblet surfaces. In particular, the plot evidences the presence of two energy containing structures at $f \approx 100 Hz$, whose time duration, in inner units, is approximately 180, corresponding to a spacing in inner units of $\Delta_x^+ = 100$, corresponding
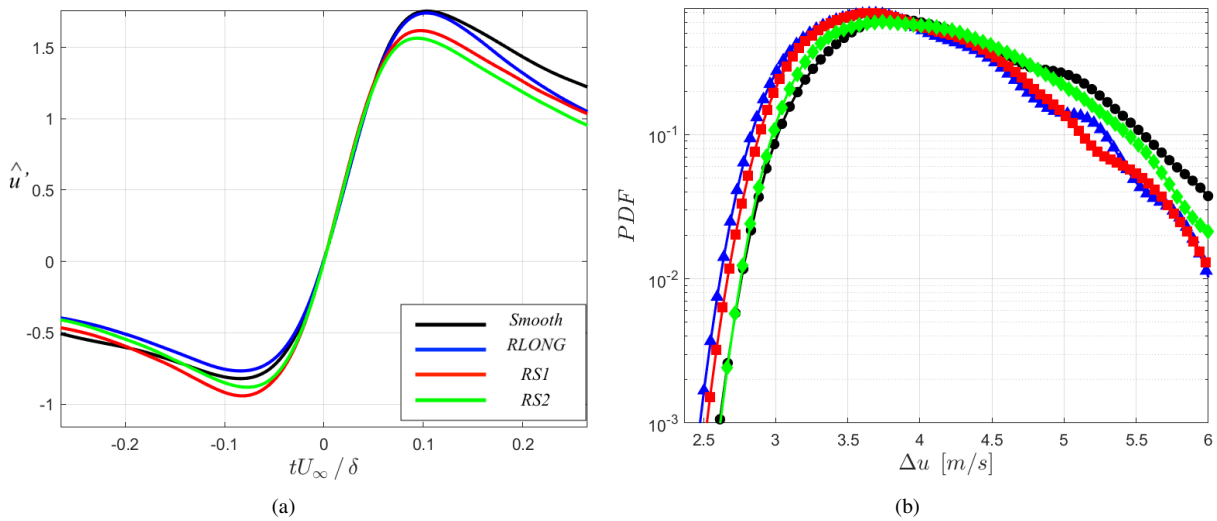
5

(a)

(b)

Fig. 3   a) VITA-averaged streamwise velocity normalised in inner units. b) Probability density function of the velocity jump over the detected VITA events. Data is collected at $Re_\theta = 2790$ and at $y^+ = 10$.
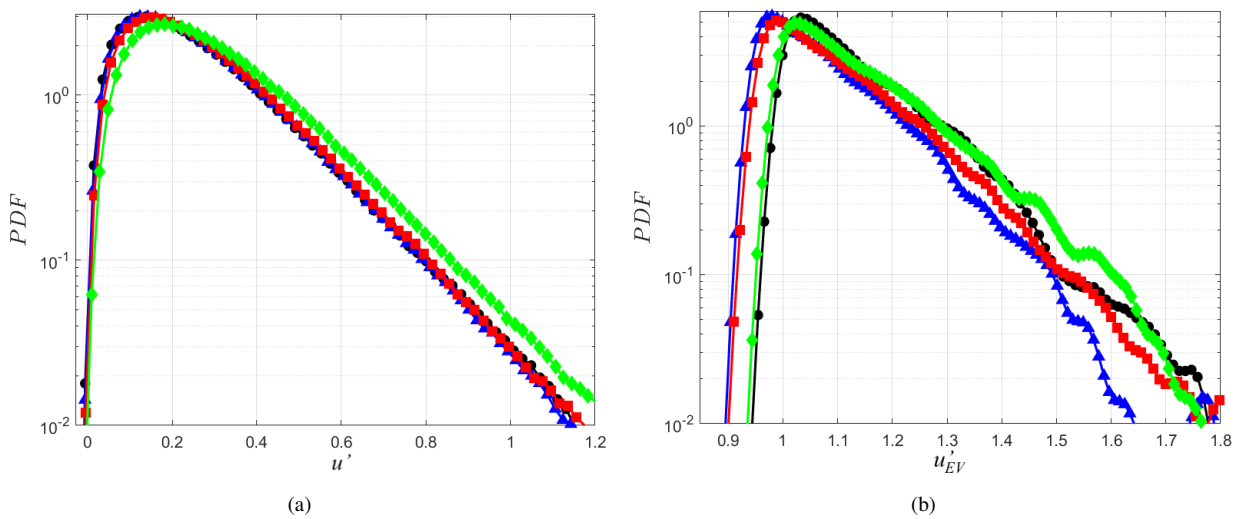

(a)

(b)

Fig. 4   Probability density function of the velocity fluctuation for the four investigated cases referred to the entire velocity signal (a) and only to the VITA events (b). Data is collected at $Re_\theta = 2790$ and at $y^+ = 10$. Lines coloring is the same of Figure 3.
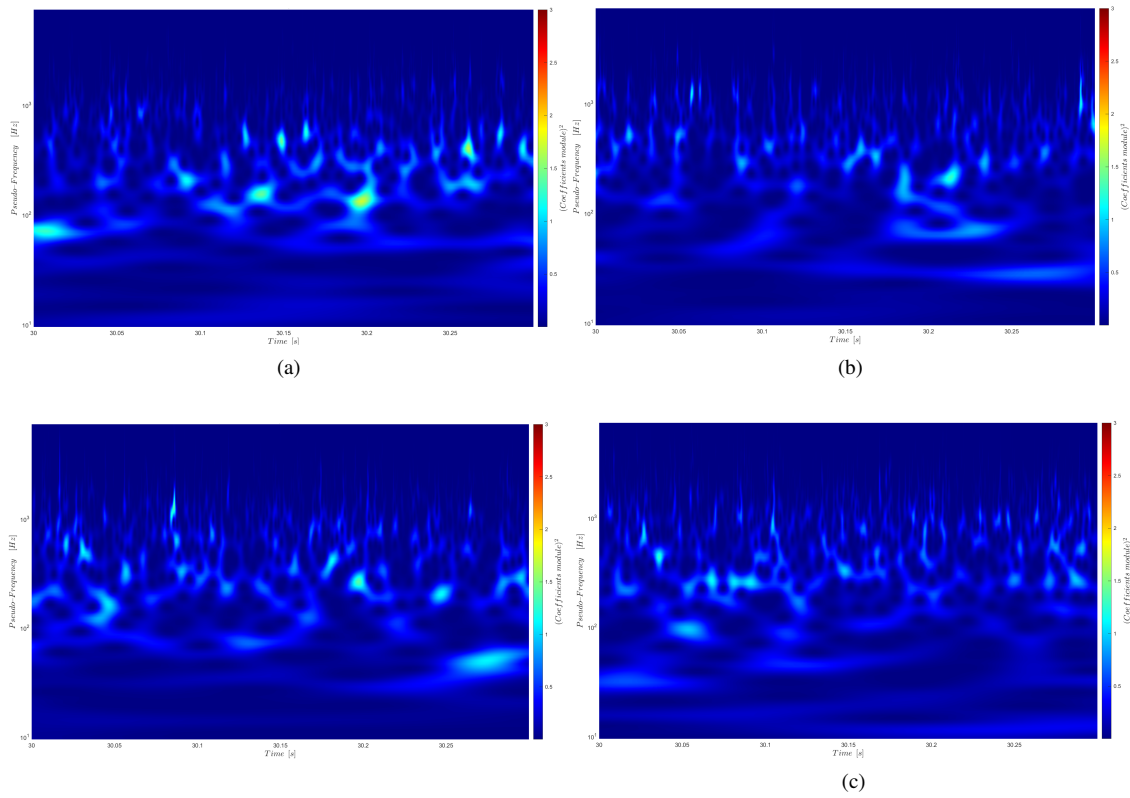
Fig. 5   Colormaps of the Wavelet Coefficients of the hot wire signal measured for the a) Smooth, b) RLONG, c) RS1 and d) RS2 cases. Data is collected at $Re_\theta = 2790$ and at $y^+ = 10$.

to the passage of the near wall structures, such as the legs of the hairpin vortices or the quasi-streamwise vortices. These structures are attenuated when the surface is manipulated with the longitudinal and the sinusoidal grooves.

This aspect, as it was also evidenced by [29] agrees with the results reported in Figure 3. The attenuation of the VITA events, which in the x-y plane are generally detected at the edges of the hairpin structures suggests that the riblet manipulation is efficient in tampering with the near wall turbulence production cycle.

Starting from the PIV images acquired in the x-y plane, we performed a low order reconstruction of the velocity field based on a subset of POD modes [30, 31], as to retain the first k modes yielding 80% of the total energy. In all the cases, $k = 20$.

The reconstructed velocity field can be expressed as:

$$\underline{\underline{U_k}} = \underline{\underline{\Psi}} \, \underline{\underline{I_k}} \, \underline{\underline{\Sigma}} \, \underline{\underline{\Phi}} = \underline{\underline{\Psi}} \, \underline{\underline{I_k}} \, \underline{\underline{\Psi}}^T \, \underline{\underline{U}} \tag{3}$$

where I_k is a diagonal square matrix of size equal to the number of snapshots with only the first k diagonal elements equal to 1 and 0 elsewhere (the resulting rank of $\underline{\underline{I_k}}$ is k); $\underline{\underline{\Psi}}$ and $\underline{\underline{\Phi}}$ represent the decomposition bases of the velocity field $\underline{\underline{U}}$ respectively in time and space and $\underline{\underline{\Sigma}}$ is the diagonal matrix containing the singular values of the velocity field.

A representative POD reconstructed instantaneous wall normal velocity field with overlaid velocity vectors for each of the investigated cases (Smooth, RLong, RS1 and RS2) is reported in Figure 6, as a colormap of the fluctuating wall normal velocity component. The contour of the wall normal velocity fluctuation is selected to highlight the existence of coherent motions associated with the displacement of momentum from the wall towards the outer region of the boundary layer and vice-versa (ejections and sweeps). In particular, positive values (in red) of the wall normal velocity are associated with an upward displacement of fluid towards the outer regions of the boundary layer (first and second quadrant), while negative values are associated with a downward displacement of fluid towards the wall, that characterizes events belonging to the third and fourth quadrants [32].

The Smooth case (Figure 6a) evidences the presence of shear layers at the interface between regions of negative and positive wall normal velocity. These regions are elongated in the streamwise direction and generate shear layers with an inclination of about 12 degrees [29].

The sinusoidal riblet cases (Figure 6c-d) are responsible for a modification of the distribution of the wall normal velocity. The first immediate observation is that the regions of large positive or negative wall normal velocity are generally orthogonal to the mean flow. Conversely, the RLong case (Figure 6b) resembles more closely the behavior already evidenced by the Smooth case.

V. Conclusion

An experimental investigation on the turbulent boundary layer structure in the presence of sinusoidal riblets has been performed through hot wire anemometry and planar particle image velocimetry. Our results suggest that the sinusoidal riblet geometry is responsible for an attenuation of the near wall structures in a zero pressure gradient turbulent boundary layer. In particular, the VITA technique allows to evidence the attenuation of the events typically detected at the edges of hairpin structures [29] when the riblet geometry is implemented.

The PIV measurements provide some insights on the reorganization of the energy containing structures in the near wall region. The instantaneous representations suggest that the wall normal motion is strongly attenuated in the case of sinusoidal riblet geometry, compared to both the smooth and the longitudinal riblet. This paves the way towards a possible interpretation of the mechanism that drives the riblet geometries: the exchange of momentum occurs with regions that are closer to the wall and that are consequently characterized by lower momentum. This gives rise to lower values of the velocity gradient at the wall, thus reducing the skin friction drag. Moreover, a more fragmented and smaller flow structure organization appear for the sinusoidal geometries.

References

[1] Iuso, G., and Onorato, M., "Turbulent boundary layer manipulation by outer-layer devices," *Meccanica*, Vol. 30, No. 4, 1995, pp. 359–376. https://doi.org/10.1007/BF00993419.

[2] Gehlert, P., Cherfane, Z., Cafiero, G., and Vassilicos, J. C., "Effect of multiscale endplates on wing-tip vortex," *AIAA Journal*, Vol. 59, No. 5, 2021. https://doi.org/10.2514/1.J059878.

[3] Cafiero, G., Castrillo, G., Greco, C. S., and Astarita, T., "On the effects of square-fractal turbulators on the flow field generated by a synthetic jet actuator," *Experimental Thermal and Fluid Science*, 2019. https://doi.org/10.1016/j.expthermflusci.2018.12.005.
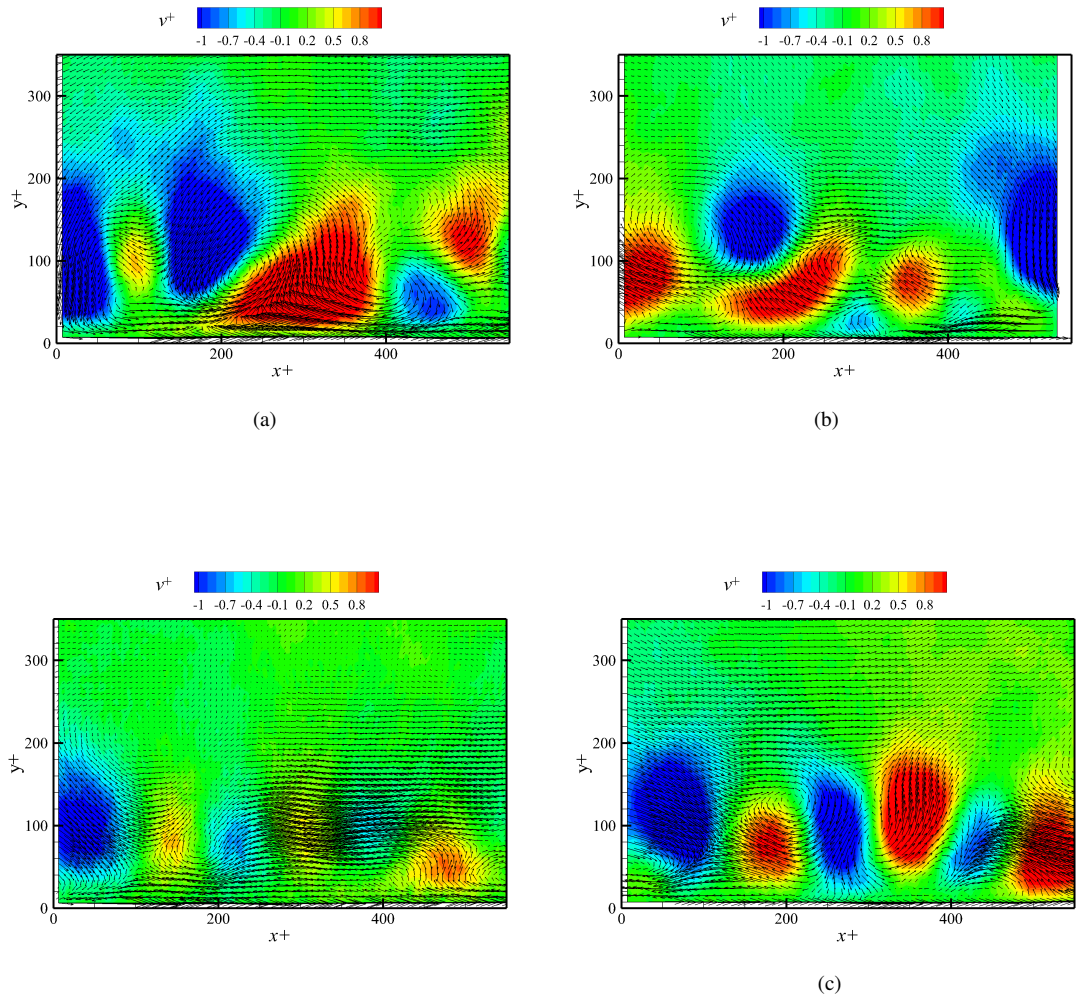
Fig. 6   Colormaps of the POD reconstructed vertical velocity fluctuation normalised in inner units, v'^+, with overlaid velocity vectors. To improve readability, one every three vectors is plotted. Data is measured at $Re_\theta = 2790$.

[4] Di Cicca, G. M., Iuso, G., Spazzini, P. G., and Onorato, M., "Particle image velocimetry investigation of a turbulent boundary layer manipulated by spanwise wall oscillations," *Journal of Fluid Mechanics*, Vol. 467, 2002, pp. 41–56. https://doi.org/10.1017/S002211200200157X.

[5] Iuso, G., Onorato, M., Spazzini, P. G., and Di Cicca, G. M., "Wall turbulence manipulation by large-scale streamwise vortices," *Journal of Fluid Mechanics*, , No. 473, 2002, pp. 23–58. https://doi.org/10.1017/S0022112002002574.

[6] Cerutti, J. J., Sardu, C., Cafiero, G., and Iuso, G., "Active flow control on a square-back road vehicle," *Fluids*, Vol. 5, No. 2, 2020. https://doi.org/10.3390/fluids5020055.

[7] Walsh, M., "Drag Characteristics of V-Groove and Transverse Curvature Riblets," *Viscous Flow Drag Reduction*, 1980, pp. 168–184. https://doi.org/10.2514/5.9781600865466.0168.0184.

[8] Walsh, M., "Turbulent boundary layer drag reduction using riblets," *AIAA Journal*, Vol. 82, No. 9, 1982, p. 0169. https://doi.org/10.2514/6.1982-169.

[9] Walsh, M. J., "Riblets as a viscous drag reduction technique," *AIAA Journal*, Vol. 21, No. 4, 1983, pp. 485–486. https://doi.org/10.2514/3.60126.

[10] Bechert, D. W., Bruse, M., Hage, W., Van Der Hoeven, J. G., and Hoppe, G., "Experiments on drag-reducing surfaces and their optimization with an adjustable geometry," *Journal of Fluid Mechanics*, Vol. 338, 1997, pp. 59–87. https://doi.org/10.1017/S0022112096004673.

[11] García-Mayoral, R., and Jiménez, J., "Drag reduction by riblets," *Philosophical Transactions of the Royal Society A: Mathematical, Physical and Engineering Sciences*, Vol. 369, No. 1940, 2011, pp. 1412–1427. https://doi.org/10.1098/rsta.2010.0359.

[12] Choi, K. S., "Near-wall structure of a turbulent boundary layer with riblets," *Journal of Fluid Mechanics*, Vol. 208, 1989, pp. 417–458. https://doi.org/10.1017/S0022112089002892.

[13] Choi, H., Moin, P., and Kim, J., "Direct numerical simulation of turbulent flow over riblets," *Journal of Fluid Mechanics*, Vol. 255, 1993, pp. 503–539. https://doi.org/10.1017/S0022112093002575.

[14] Bechert, D. W., Bruse, M., Hage, W., and Meyer, R., *Fluid mechanics of biological surfaces and their technological application*, Vol. 87, 2000. https://doi.org/10.1007/s001140050696.

[15] Sha, T., Itoh, M., Tamano, S., Yokota, K., and Akio, N., "207 Experimental Study on Drag Recduction in Turbulent Flow on Zigzag Riblet Surface," *The Proceedings of the Fluids engineering conference*, Vol. 2005, No. 0, 2005, p. 21. https://doi.org/10.1299/jsmefed.2005.21.

[16] Peet, Y., Sagaut, P., and Charron, Y., "Turbulent drag reduction using sinusoidal riblets with triangular cross-section," *38th AIAA Fluid Dynamics Conference and Exhibit*, 2008. https://doi.org/10.2514/6.2008-3745.

[17] Peet, Y., and Sagaut, P., "Theoretical prediction of turbulent skin friction on geometrically complex surfaces," *Physics of Fluids*, Vol. 21, No. 10, 2009. https://doi.org/10.1063/1.3241993.

[18] Sasamori, M., Mamori, H., Iwamoto, K., and Murata, A., "Experimental study on drag-reduction effect due to sinusoidal riblets in turbulent channel flow," *Experiments in Fluids*, Vol. 55, No. 10, 2014. https://doi.org/10.1007/s00348-014-1828-z.

[19] Sasamori, M., Iihama, O., Mamori, H., Iwamoto, K., and Murata, A., "Parametric Study on a Sinusoidal Riblet for Drag Reduction by Direct Numerical Simulation," *Flow, Turbulence and Combustion*, Vol. 99, No. 1, 2017, pp. 47–69. https://doi.org/10.1007/s10494-017-9805-2.

[20] Choi, K. S., "Near-wall structure of turbulent boundary layer with spanwise-wall oscillation," *Physics of Fluids*, Vol. 14, No. 7, 2002, pp. 2530–2542. https://doi.org/10.1063/1.1477922.

[21] Cannata, M., Cafiero, G., and Iuso, G., "Large-scale forcing of a turbulent channel flow through Spanwise synthetic jets," *AIAA Journal*, Vol. 58, No. 5, 2020, pp. 2042–2052. https://doi.org/10.2514/1.J059047.

[22] Hutchins, N., Nickels, T. B., Marusic, I., and Chong, M. S., "Hot-wire spatial resolution issues in wall-bounded turbulence," *Journal of Fluid Mechanics*, Vol. 635, 2009, pp. 103–136. https://doi.org/10.1017/S0022112009007721.

[23] Mendez, M. A., Raiola, M., Masullo, A., Discetti, S., Ianiro, A., Theunissen, R., and Buchlin, J. M., "POD-based background removal for particle image velocimetry," *Experimental Thermal and Fluid Science*, Vol. 80, 2017, pp. 181–192. https://doi.org/10.1016/j.expthermflusci.2016.08.021.

[24] Astarita, T., "Analysis of interpolation schemes for image deformation methods in PIV: Effect of noise on the accuracy and spatial resolution," *Experiments in Fluids*, Vol. 40, No. 6, 2006, pp. 977–987. https://doi.org/10.1007/s00348-006-0139-4.

[25] Astarita, T., "Analysis of velocity interpolation schemes for image deformation methods in PIV," *Experiments in Fluids*, Vol. 45, No. 2, 2008, pp. 257–266. https://doi.org/10.1007/s00348-008-0475-7.

[26] Astarita, T., "Analysis of weighting windows for image deformation methods in PIV," *Experiments in Fluids*, Vol. 43, No. 6, 2007, pp. 859–872. https://doi.org/10.1007/s00348-007-0314-2.

[27] Blackwelder, R. F., and Kaplan, R. E., "On the wall structure of the turbulent boundary layer," *Journal of Fluid Mechanics*, Vol. 76, No. 1, 1976, pp. 89–112. https://doi.org/10.1017/S0022112076003145.

[28] Farge, M., "Wavelet transforms and their applications to turbulence," *Annual Review of Fluid Mechanics*, Vol. 24, No. 1, 1992, pp. 395–457. https://doi.org/10.1146/annurev.fluid.24.1.395.

[29] Adrian, R. J., Meinhart, C. D., and Tomkins, C. D., "Vortex organization in the outer region of the turbulent boundary layer," *Journal of Fluid Mechanics*, Vol. 422, 2000, p. 1–54. https://doi.org/10.1017/S0022112000001580.

[30] Sirovich, L., "Turbulence and the dynamics of coherent structures: I, II, III," *Q Appl Math*, Vol. 45, 1987, pp. 561–590.

[31] Raiola, M., S., D., and A., I., "On PIV random error minimization with optimal POD-based low-order reconstruction," *Experiments in Fluids*, Vol. 56, 2015, p. 75.

[32] Wallace, J. M., "Quadrant Analysis in Turbulence Research: History and Evolution," *Annual Review of Fluid Mechanics*, Vol. 48, 2016, pp. 131–158. https://doi.org/10.1146/annurev-fluid-122414-034550.